Stationary temperature profiles in a liquid nanochannel: Comparisons between molecular-dynamics simulation and classical hydrostatics

Hisashi Okumura*
Department of Physics, School of Science, Nagoya University, Furo-cho, Chikusa-ku, Nagoya, Aichi 464-8602, Japan

David M. Heyes†
Division of Chemistry, School of Biomedical and Molecular Sciences, University of Surrey, Guildford GU2 7XH, United Kingdom
(Received 9 April 2006; revised manuscript received 26 September 2006; published 1 December 2006)

We compare the results of three-dimensional molecular-dynamics (MD) simulations of a Lennard-Jones (LJ) liquid with a hydrostatic (HS) solution of a high temperature liquid channel which is surrounded by a fluid at lower temperature. The maximum temperature gradient, dT/dx, between the two temperature regions ranged from ∞ (step function) to $dT/dx=0.1$ (in the usual LJ units). Because the systems were in stationary-nonequilibrium states with no fluid flow, both MD simulation and the HS solution gave flat profiles for the normal pressure in all temperature-gradient cases. However, the other quantities showed differences between the two methods. The MD-derived density was found to oscillate over the length of ca. 8 LJ particle diameters from the boundary plane in the system with the infinite temperature gradient, while the HS-derived density showed simply a stepwise profile. The MD simulation also showed another anomaly near the boundary in potential energy. We have found systems in which the HS treatment works well and those where the HS approach breaks down, and therefore established the minimum length scale for the HS treatment to be valid. We also compare the kinetic temperature and the configurational temperature in these systems, and show that these can differ in the transition zone between the two temperatures.

DOI: 10.1103/PhysRevE.74.061201 PACS number(s): 65.20.+w, 02.70.Ns, 47.85.Dh, 05.70.Ln

I. INTRODUCTION

There are various methods that can be used to study liquid behavior by computer simulation. One method is molecular dynamics (MD), which applies Newton's equations of motion to an assembly of interacting model molecules. This method uses parameters attributable to individual molecules and the intermolecular forces between them as the starting point. Another method is based on the continuum hydrodynamics (HD) or hydrostatics (HS) equations, such as the Navier-Stokes equation. The MD and HD/HS methods start from the opposite ends of the length-scale spectrum. It is reasonable to assume that there will be an intermediate length scale in which both methods are of equal utility, above which HD/HS is best and below which MD is only truly valid. Quite what this length scale is, is still an issue of debate, and probably depends somewhat on the details and processes of the systems being followed.

Many studies have been carried out to compare these two approaches for the same nonequilibrium fluid system or to produce a hydrodynamic behavior by MD simulations: [1–21]. For example, convective flows such as Rayleigh-Bénard convection [1–4] and Taylor vortex [5,6] have been observed by MD simulation. Qualitative comparisons of the MD simulations with the HD calculations have been made as for the stationary Rayleigh-Bénard convections [3,4]. Shock-wave structure has been simulated, too [7–9]. The MD-derived profiles of density, pressure, temperature, and energy in the stationary shock wave agree with those by the HD calculations. Molecular dynamics simulations for nonstationary thermal processes have also been compared with corresponding HD calculations [10]. The temporal and spatial profiles of all five fields of temperature T, mass density ρ, pressure P, potential energy U, and fluid velocity v by the two methods showed good agreement. In addition to these one-phase flows, a two-phase flow consisting of a liquid and a gas has been studied. Nonstationary dynamics of a bubble was observed by MD simulation [11,12]. The MD-derived bubble dynamics agrees well with that by the hydrodynamic Rayleigh-Plesset equation [12]. These studies showed good agreement between the MD simulations and the HD/HS calculations. There are also several publications that reveal differences between the outcomes of these two methods [13–15]. Poiseuille flow between two plates has also been investigated by MD simulations [13–15]. Although a stationary velocity profile is quadratic, just as for the HD prediction, if the channel width is of the order of 30 atomic diameters, the MD-derived velocity profile deviates from the hydrodynamic prediction for the channel width of 5 or less atomic diameters.

In contrast, there is no work that compares the MD and HD/HS treatments systematically for all five fields of T, ρ, P, U, and v through the transition states in which the HD/HS treatment works well to that where it breaks down. An important question is therefore how small does the system have to be before the coarse-grained HD/HS approach is no longer valid, and MD is required? In order to answer this question, a systematic comparison between MD and HD/HS treatments is necessary considering several sizes spanning the likely transition regime. The purpose of this work is to make such a comparison, using different temperature profiles with various degrees of localization. We construct a nonequilib-

*Electronic address: hokumura@tb.phys.nagoya-u.ac.jp
†Electronic address: d.heyes@surrey.ac.uk

 ©2006 The American Physical Society

rium Lennard-Jones (LJ) liquid system which has two essentially flat temperature regions. We compare three systems distinguished by different characteristic temperature gradients in the transitional zone between the two regions. In the HS treatment all five fields of temperature T, mass density ρ, pressure P, potential energy U, and fluid velocity v were used. The HS data are compared with those produced by a corresponding MD treatment. Such a local heating is in principle possible by laser-heating, although the steep temperature gradients used in our simulations would probably be difficult to achieve experimentally. Laser heating is applied widely, for example, inducing convective flows in fluidics [22] and microbubble formation to damage tissue selectively in medical science [23]. The present computational approach to a heated fluid on a molecular level could be useful in helping design practical applications.

The outline of this paper is as follows. In Sec. II we describe the computational details of the MD simulation and the HS calculation. In Sec. III the results and discussions are presented. Concluding remarks follow in Sec. IV.

II. METHODS

A. Molecular-dynamics simulations

We have performed MD simulations using the Lennard-Jones 12-6 potential,

$$\phi(r) = 4\epsilon\left[\left(\frac{\sigma}{r}\right)^{12} - \left(\frac{\sigma}{r}\right)^{6}\right], \tag{1}$$

where ϵ and σ set the energy and length scales of the system, respectively. In the following discussion, length, energy, and mass are scaled in units of the Lennard-Jones diameter σ, the minimum value of the potential ϵ, and the atom mass m.

The number of particles N in the cubic unit cell was 100 000, with the usual periodic boundary conditions applied in the x, y, and z direction. The sidelength of the cubic simulation box was $L=50$, therefore the volume of the box was $V=125\,000$ and the average number-density in the whole box was $\rho=0.80$. The densities and temperatures employed here are in the liquid phase of the Lennard-Jones 12-6 fluid [24,25]. The interaction cutoff radius r_c was taken as 4.0, and cutoff corrections were added to the interaction-related quantities such as pressure and potential energy.

In order to calculate the distribution of the fields such as temperature $T(x)$, the simulation box was resolved into 500 segments along the x axis; therefore the sliced segment length was $\Delta x=0.1$. The kinetic temperature T_{knt} in the kth sliced segment was given by

$$T_{\mathrm{knt}} = \left\langle \frac{1}{3k_{\mathrm{B}}N_k}\sum_{i\in k}\frac{(\boldsymbol{p}_i-\boldsymbol{p}_0)^2}{m_i}\right\rangle, \tag{2}$$

where k_{B} is Boltzmann's constant and N_k is a number of particles in the kth sliced segment. The average momentum $\boldsymbol{p}_0$ of the model molecules in the slice is given by $\boldsymbol{p}_0 = \frac{1}{N_k}\Sigma_{i\in k}\boldsymbol{p}_i$. The brackets $\langle\cdots\rangle$ denote a time average.

The Nosé-Hoover thermostat for temperature control was employed here [26–28]. The equations of motion for the coordinate $\boldsymbol{r}_i$, momentum $\boldsymbol{p}_i$, and variable ξ for the Nosé-Hoover thermostat are given by

$$\dot{\boldsymbol{r}}_i = \frac{\boldsymbol{p}_i}{m_i}, \tag{3}$$

$$\dot{\boldsymbol{p}}_i = \boldsymbol{F}_i - \xi_k\boldsymbol{p}_i, \tag{4}$$

$$\dot{\xi}_k = \frac{1}{Q}\left[\sum_{i\in k}\frac{1}{m_i}(\boldsymbol{p}_i-\boldsymbol{p}_0)^2 - 3N_k k_{\mathrm{B}}T_k\right], \tag{5}$$

where k is the index of the slice which includes the particle i, $\boldsymbol{F}_i$ is the force acting on the particle i, Q is the artificial "mass" associated with ξ_k, and T_k is the temperature in the kth sliced segment. The equations of motion in Eqs. (3)–(5) were integrated by the time-reversible algorithm proposed by Martyna *et al.* [29]. The time step was set to $\Delta t=0.01$. The stationary states were established over a 20 000 time step equilibration run. Data collection was taken over a further 20 000 MD time steps.

A stationary state was established in the simulation cell along the x-direction which consisted of a flat or near-flat high temperature region and a low temperature region. The high temperature region was thermostated at $T_{\mathrm{h}}=2$ and the low temperature region was set as $T_{\mathrm{l}}=1$. The difference between the two temperatures was therefore $T_{\mathrm{h}}-T_{\mathrm{l}}=1$, i.e., quite large compared with normal thermal values. The temperature profile was set up according to the hyperbolic tangent function,

$$T(x) = \begin{cases} 1.5 + 0.5\tanh[(x-0.25L)/a], & \text{if } x \le 0.5L, \\ 1.5 + 0.5\tanh[-(x+0.75L)/a], & \text{if } x > 0.5L, \end{cases} \tag{6}$$

where a is a parameter that characterizes the distance range of the transition in the temperature profile. Twice the value of the parameter a is roughly the range of the transition between the high and low temperatures, in the LJ reduced units. To clarify this, consider a straight line that has the same temperature gradient dT/dx as that in Eq. (6) at $x/L=0.25$. The distance between the position x at which this straight line takes $T_{\mathrm{h}}=2$ and that at which this straight line is $T_{\mathrm{l}}=1$ is $2a$. The cases of $a=0$, 1, and 5 were investigated. The temperature profiles for the three values of a are illustrated in Fig. 1. The temperature is controlled well as in Eq. (6) by the Nosé-Hoover thermostat. In the case of $a=0$ [Fig. 1(a)], the temperature profile is a step function, with an infinite temperature gradient at the boundary, i.e., $dT/dx=\infty$. The system with $a=1$, shown in Fig. 1(b), has an intermediate typical temperature gradient; its maximum temperature gradient is $dT/dx=0.5$. The temperature gradient in the system with $a=5$, given in Fig.1(c), had the most gradual temperature transition zone of the calculations, and its maximum temperature gradient was 0.1.

Among the works comparing the two techniques, most of them have focused on systems with a solid wall such as the Poiseuille flow [13,14]. Although these systems are clearly important, hydrostatics needs an additional approximation to deal with the interface between the fluid and the solid wall

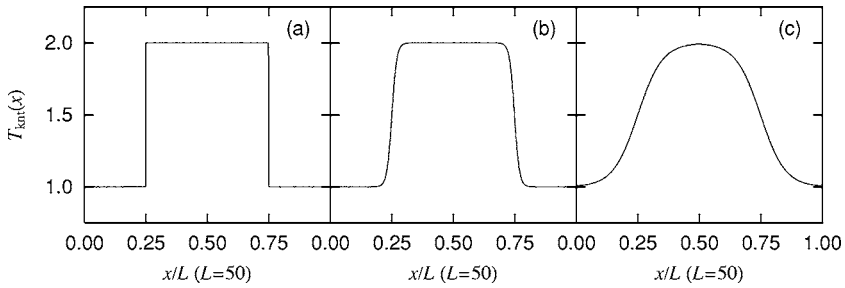

FIG. 1. Distributions of kinetic temperature T_{knt} in the x direction, which is controlled by the Nosé-Hoover thermostat. This temperature profile is set according to the hyperbolic tangent function in Eq. (6). The parameter a characterizes the distance range of the transition in the temperature profile: (a) in the case of $a=0$, (b) for $a=1$, and (c) for $a=5$.

such as the no slip condition. The intention here was to exclude the need for such a secondary approximation for the interface and to focus entirely on the essential nature of the continuum approximation for the hydrostatics. This is why the chosen model for the nonequilibrium system had the temperature gradient shown in Fig. 1 but for a fluid-fluid system, i.e., without a solid interface.

B. Hydrostatics calculations

Hydrostatics calculations were performed to match as closely as possible the MD states. The sidelength of the cubic simulation cell was the same, $L=50$, with the usual periodic boundary conditions in all three directions. The space was decomposed into 500 segments along the x axis. The one-dimensional Navier-Stokes equation, given by

$$\frac{\partial \rho v}{\partial t} + \frac{\partial P}{\partial x} + \frac{\partial (\rho v^2)}{\partial x} - \frac{\partial}{\partial x}\left[\left(\frac{4}{3}\eta + \zeta\right)v_x\right] = 0, \qquad (7)$$

where η is shear viscosity, ζ is bulk viscosity, and suffixes x of v means x derivative, is the relevant equation. Because our systems were stationary states with no fluid flow, $v = 0$, the Navier-Stokes equation in Eq. (7) can be simplified to the time independent equation,

$$\frac{\partial P}{\partial x} = 0. \qquad (8)$$

That is, the pressure was predicted to be constant with x. Therefore we do not need the transport coefficients such as η and ζ, and only the equations of state are needed to establish the relationships between T, ρ, P, and U and their various profiles with x.

The procedure to obtain the HS thermodynamic property profiles was as follows. The density profile was determined so that pressure profile would be constant across the cell for the temperature-profile of Eq. (6) and for the average density of $\rho=0.8$. First, a temporary pressure profile $P(x)$ was proposed which was independent of x. Subject to the temperature profile, $T(x)$ given in Eq. (6), a density profile was calculated as a function of the temporary temperature and pressure, $\rho(x)=\rho[T(x),P(x)]$, from the equation of state. The temporary average density ρ' was obtained by integrating this density profile as $\rho' = \frac{1}{L}\int_0^L dx \rho(x)$. If ρ' was higher than its appropriate value of $\rho=0.8$, the temporary pressure was reset to a lower value, or if ρ' was lower than $\rho=0.8$, the temporary pressure was reset higher. This procedure was repeated for the reset temporary pressure until the average density converged to its appropriate value. After obtaining the appropriate profiles of $\rho(x)$and $P(x)$, the profile of $U(x)$ was calculated as a function of temperature and density as $U(x) = U[T(x),\rho(x)]$ again from the equation of state.

Five equations of the HD/HS, equation for mass transfer, equation for momentum transfer (the Navier-Stokes equation), equation for energy transfer, equation of states for pressure $P=P(T,\rho)$, and equation of states for potential energy $U=U(T,\rho)$ are normally used to determine five fields of T, ρ, P, U, and v. In our case, the temperature profile $T(x)$ is given and the fluid velocity is fixed to zero at all points, i.e., $v=0$, which means that the number of variables is less by two than that for a system in which temperature is not given and fluid velocity is not fixed. Therefore we did not have to use the equation for mass transfer and equation for energy transfer here. Three HS equations set, the Navier-Stokes equation, the equation of state for pressure $P=P(T,\rho)$, and the equation of state for potential energy $U=U(T,\rho)$, were sufficient.

There are some equations of state that are moderately accurate over a wide range of T and ρ [30,31]. For example, Johnson *et al.* fitted the MD and Monte Carlo data in the ranges of $T=0.7-6.0$ and $\rho=0.005-1.25$ [30]. Although they are useful, an equation of state that is more accurate in the specific ranges of $T=1.0-2.0$ and $\rho=0.7-0.9$ was sought. Consequently MD simulations were performed to determine accurately the equation of state for $P=P(T,\rho)$ and $U=U(T,\rho)$ in this region. Canonical MD simulations were carried out by the Nosé-Hoover thermostat [26–28] in the temperature range of $T=1.0-2.0$ with the interval of $\Delta T=0.2$ in the density range of $\rho=0.70-0.90$ with the interval of $\Delta\rho=0.4$. The number of particles N was 1000. The equations of motion were integrated for 10 000MD steps with $\Delta t=0.01$. For the estimation of the statistical uncertainties, the simulation time steps were divided into two parts of 5000 MD steps and P and U calculated in each part. Error bars were determined from the standard deviations of these data. The values of P and U are given in Table I. These values were used with a linear interpolation for intermediate T and ρ values as follows:

TABLE I. Pressure P and potential energy per particle U at several values of temperature and density estimated by the MD simulations. The numbers in parentheses are the estimated uncertainties.

T	ρ	P	U
1.0	0.82	1.370(7)	−5.646(1)
1.0	0.86	2.218(5)	−5.860(1)
1.0	0.90	3.324(1)	−6.046(1)
1.2	0.78	1.633(1)	−5.245(1)
1.2	0.82	2.386(1)	−5.462(1)
1.2	0.86	3.377(13)	−5.653(2)
1.2	0.90	4.639(10)	−5.813(2)
1.4	0.74	1.817(2)	−4.867(1)
1.4	0.78	2.483(6)	−5.088(1)
1.4	0.82	3.357(2)	−5.285(1)
1.4	0.86	4.468(3)	−5.457(1)
1.4	0.90	5.873(3)	−5.595(1)
1.6	0.70	1.902(2)	−4.516(1)
1.6	0.74	2.514(3)	−4.735(1)
1.6	0.78	3.287(1)	−4.937(1)
1.6	0.82	4.256(2)	−5.121(1)
1.6	0.86	5.493(17)	−5.273(4)
1.8	0.70	2.499(4)	−4.401(1)
1.8	0.74	3.172(7)	−4.610(1)
1.8	0.78	4.048(1)	−4.796(1)
1.8	0.82	5.139(5)	−4.960(2)
2.0	0.70	3.063(4)	−4.289(1)
2.0	0.74	3.818(7)	−4.488(1)
2.0	0.78	4.781(3)	−4.660(1)

$$f(x,y) = (1-x)(1-y)f(0,0) + x(1-y)f(1,0) + (1-x)yf(0,1) + xyf(1,1). \quad (9)$$

Here $f(x,y)$ is the value of P or U at

$$x = (T - T_n)/\Delta T, \quad (10)$$

$$y = (\rho - \rho_n)/\Delta\rho, \quad (11)$$

where T_n and ρ_n are the data points for the MD simulation not larger than T and ρ, respectively. The ranges of x and y are $0 < x \leq 1$ and $0 < y \leq 1$, respectively. The values of $P(T,\rho)$ and $U(T,\rho)$ at the four corners are expressed by $f(0,0)$, $f(1,0)$, $f(0,1)$, and $f(1,1)$. Not only at the corners of $(x,y)=(0,0)$, (1,0), (0,1), and (1,1), but also on the lines of $x=0$, $x=1$, $y=0$, and $y=1$, $f(x,y)$ is continuous in Eq. (9). To fit the MD data more smoothly, a higher order fitting equation such as the third or fifth formula [32] can be used. For the present work, however, the linear formula in Eq. (9) was sufficient.

III. RESULTS AND DISCUSSION

The density profiles, $\rho(x)$, are shown in Fig. 2. They were calculated from

$$\rho = \left\langle m_i \frac{N_k}{V_k} \right\rangle, \quad (12)$$

where V_k is a volume of the kth segment. In the case of $a=5$, the density profile like the temperature profile is smooth, as shown in Fig. 2(c). The agreement between the density profiles by the MD simulation (solid line) and the HS calculation (dotted curve) is very good and they are hardly distinguishable on the figure. The differences between the MD and HS treatments start to be seen in the case of $a=1$, as seen in Fig. 2(b). The density profile calculated by the MD simulation is not as steep as from the HS calculation. In the case of $a=0$, the density profile calculated by the HS is a step function just as for the temperature distribution given in Eq. (6). In marked contrast, the MD-derived density profile is highly oscillatory near the sharp temperature change boundaries as shown in Fig. 2(a). The oscillations are in both the low and high temperature regimes. The distance between adjacent peaks is approximately the LJ particle diameter, indicating a "layering" of the particles near the boundaries, which is observed only in the MD simulations. The oscillation is seen for about four diameters in the high temperature region and four diameters again in the low temperature region. The oscillations exist over about eight diameters in total per boundary. The height of the peaks decreases with distance from the

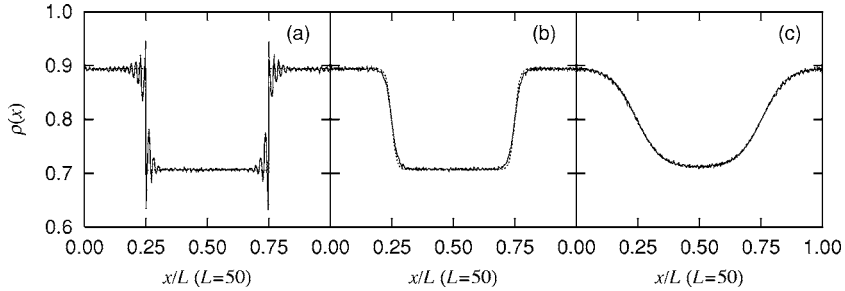

FIG. 2. Distributions of density ρ in the x direction for (a) $a=0$, (b) $a=1$, and (c) $a=5$. The solid and dotted lines represent the profiles from the MD simulations and HS calculations, respectively. In the case of $a=5$, the agreement between the density profiles from the two approaches is very good. In the case of $a=0$, the density profile calculated by the HS is a step function, whereas the MD-derived density profile has oscillations near the boundaries.

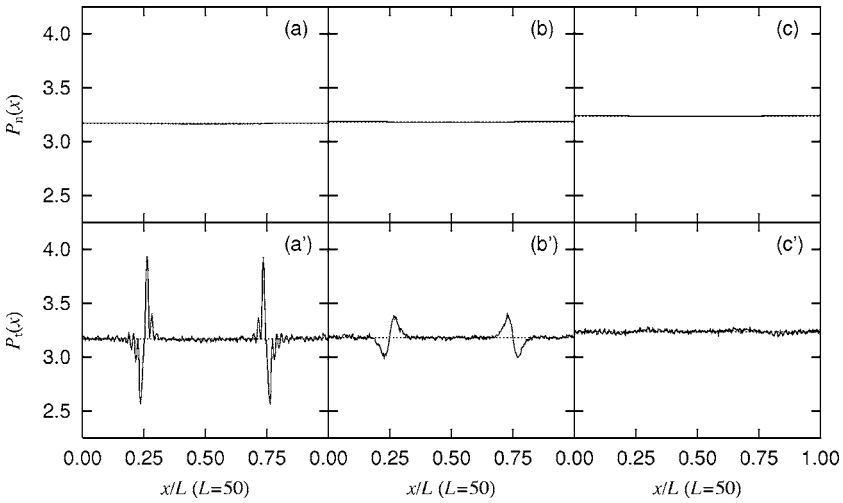

FIG. 3. (a)–(c) Distributions of the normal components of pressure P_n and (a′)–(c′) those of the transverse components P_t given by the coarse-grained Irving-Kirkwood expression in Eq. (14). See the caption of Fig. 2 for the details. The normal components of pressure P_n are constant with x in all temperature-profile cases.

boundary. Density oscillations in a liquid are typical in the boundary region between a solid and a liquid [33–35], and between two immiscible liquids [36]. Although our system consists of one type of molecule, there is a sufficiently large and sharp density difference between the two temperature regions in the $a=0$ case, that the liquid behaves as if it were two different liquids with distinct densities in contact with each other. This is why it tends to layer in contrast to the systems where $a>0$.

The pressure tensor, $\mathbf{P}$, in an inhomogeneous liquid has been evaluated with the Irving-Kirkwood expression [37]. After Irving and Kirkwood, alternative computational techniques have been studied to make the original Irving-Kirkwood expression more suitable for MD or Monte Carlo simulations [15,38]. Todd *et al.* reformulated the Irving-Kirkwood expression for the normal component of pressure and derived the method of plane technique [15]. $\mathbf{P}$ is given by

$$\mathbf{P}(x) = \left\langle \frac{1}{A}\sum_i \frac{(\boldsymbol{p}_i-\boldsymbol{p}_0)(\boldsymbol{p}_i-\boldsymbol{p}_0)}{m_i}\delta(x_i-x)\right\rangle - \left\langle \frac{1}{2A}\sum_i\sum_{j\neq i}\frac{\boldsymbol{r}_{ij}\boldsymbol{r}_{ij}}{r_{ij}}\frac{\partial\phi(r_{ij})}{\partial r_{ij}}\frac{1}{|x_{ij}|}\theta\left(\frac{x-x_i}{x_j-x_i}\right)\theta\left(\frac{x_j-x}{x_j-x_i}\right)\right\rangle, \tag{13}$$

where θ denotes the Heaviside step function and A is the cross-section area which is normal to the x-axis. Here, $\boldsymbol{r}_{ij}$ is a vector from one particle at $\boldsymbol{r}_i$ to another at $\boldsymbol{r}_j$: $\boldsymbol{r}_{ij}=\boldsymbol{r}_i-\boldsymbol{r}_j$, r_{ij} is its distance: $r_{ij}\equiv|\boldsymbol{r}_{ij}|$, and $(\boldsymbol{p}_i-\boldsymbol{p}_0)(\boldsymbol{p}_i-\boldsymbol{p}_0)$ and $\boldsymbol{r}_{ij}\boldsymbol{r}_{ij}$ are dyadic tensors. For the pressure calculation in the binned space, the coarse-grained expression of Eq. (13) proposed by Ikeshoji *et al.* is appropriate [39,40]. The pressure tensor $\mathbf{P}$ in the kth sliced segment is given by

$$\mathbf{P} = \left\langle \frac{1}{V_k}\sum_{i\in k}\frac{(\boldsymbol{p}_i-\boldsymbol{p}_0)(\boldsymbol{p}_i-\boldsymbol{p}_0)}{m_i}\right\rangle - \left\langle \frac{1}{2V_k}\sum_i\sum_{j\neq i}\frac{\boldsymbol{r}_{ij}\boldsymbol{r}_{ij}}{r_{ij}}\frac{\partial\phi(r_{ij})}{\partial r_{ij}}\frac{\delta x}{|x_{ij}|}\right\rangle, \tag{14}$$

where δx is a length of the part of the line segment between x_i and x_j which penetrates the kth slice. For the sake of simplicity, let us suppose x_j is larger than x_i (δx is also easily calculated in a similar way in the case that x_i is larger than x_j) and regard the x-coordinate at the boundary between the $(k-1)$th and kth slices as $x_{k-1/2}$ and that between the kth and $(k+1)$th slices as $x_{k+1/2}$. If the line segment between x_i and x_j penetrates through the kth slice from $x_{k-1/2}$ to $x_{k+1/2}$, $\delta x=\Delta x$. If this line segment does not go through the kth slice at all, $\delta x=0$. If this line segment partially penetrates in the kth slice, δx is a length that the line segment occupies in the kth segment ($0<\delta x<\Delta x$). In other words, if both particles i and j are in the kth slice, $\Delta x=|x_j-x_i|$, if only the particle i is in the kth slice and $x_j>x_{k+1/2}$, $\Delta x=x_{k+1/2}-x_i$, and if only the particle j is in the kth slice and $x_i<x_{k-1/2}$, $\Delta x=x_j-x_{k-1/2}$. The normal component $P_n(x)$

$$P_n(x) = P_{xx}(x) \tag{15}$$

and the transverse component $P_t(x)$ of the pressure tensor

$$P_t(x) = \frac{1}{2}\left[P_{yy}(x)+P_{zz}(x)\right] \tag{16}$$

are shown in Fig. 3. The normal component of the pressure $P_n(x)$ is constant with x for all values of a, and agrees well with the HS-derived pressure profile. This demonstrates that the MD-derived normal pressure satisfies the HS condition of "no flow" even at the molecular scale. On the other hand, the transverse component of the pressure $P_t(x)$ has positive peaks on the high temperature side and negative peaks on the low temperature side near the boundary. In the case of $a=0$ as shown in Fig. 3(a′), the MD-derived $P_t(x)$ shows oscillations near the boundary, mirroring those in the density profile. As the parameter a increases, these peak become lower. In the case of $a=5$, the MD pressure profile is nearly constant as shown in Fig. 3(c′). These features in the pressure are quite similar to those observed for the liquid-gas interface [38,40]. Some peaks have been also observed in $P_t(x)$, whereas $P_n(x)$ is constant at the liquid-gas interface.

If one simply "bins" the usual definition of the bulk pressure, this is correct only for a homogeneous liquid but not for

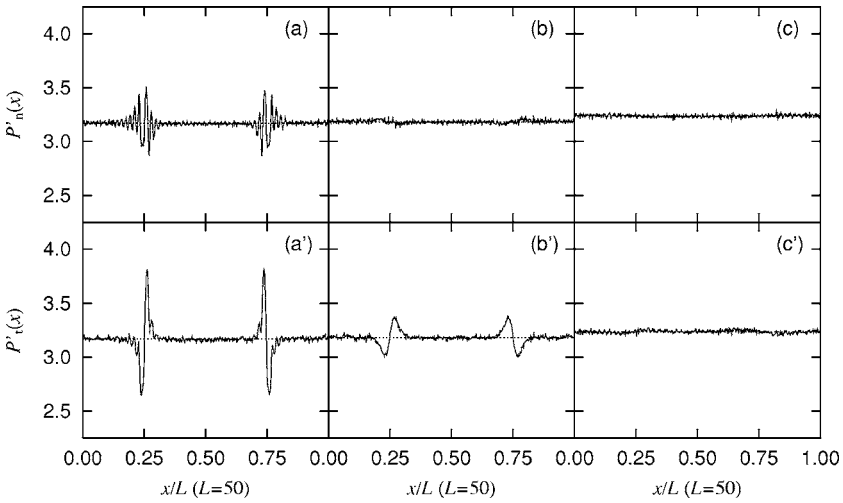

FIG. 4. (a)–(c) Distributions of the normal components of pressure P'_n and (a′)–(c′) those of the transverse components P'_t given by the approximate formula in Eq. (18). See the caption of Fig. 2 for the details. There are artifactual oscillations near the boundaries in $P'_n(x)$.

an inhomogeneous liquid studied here. This approximate pressure tensor is given by

$$\mathbf{P}'(x) = \left\langle \frac{1}{A}\sum_i \frac{(\boldsymbol{p}_i - \boldsymbol{p}_0)(\boldsymbol{p}_i - \boldsymbol{p}_0)}{m_i}\delta(x_i - x)\right\rangle - \left\langle \frac{1}{2A}\sum_i \sum_{j\neq i} \frac{\boldsymbol{r}_{ij}\boldsymbol{r}_{ij}}{r_{ij}}\frac{\partial\phi(r_{ij})}{\partial r_{ij}}\delta(x_i - x)\right\rangle. \quad (17)$$

For the comparison with the true pressure tensor calculated by Eq. (14), we also calculated this approximate pressure. The actual calculation was performed by the coarse-grained expression as in Eq. (14):

$$\mathbf{P}' = \left\langle \frac{1}{V_k}\sum_{i\in k} \frac{(\boldsymbol{p}_i - \boldsymbol{p}_0)(\boldsymbol{p}_i - \boldsymbol{p}_0)}{m_i}\right\rangle - \left\langle \frac{1}{2V_k}\sum_{i\in k}\sum_{j\neq i} \frac{\boldsymbol{r}_{ij}\boldsymbol{r}_{ij}}{r_{ij}}\frac{\partial\phi(r_{ij})}{\partial r_{ij}}\right\rangle. \quad (18)$$

Bear in mind that the prime notation indicates an approximate expression of the pressure profile. The normal component $P'_n(x)$ and transverse component $P'_t(x)$ of the approximate pressure tensor calculated by Eq. (18) are shown in Fig. 4. In this case, not only $P'_t(x)$ but also $P'_n(x)$ shows oscillations near the boundaries, as shown in Fig. 4(a). The oscillations in $P'_n(x)$ are artifacts, similar to those observed, for example, at the solid-liquid interface [15]. The pressure tensor calculated by Eq. (17) or Eq. (18) is only an approximation to the true local pressure which must be evaluated by the Irving-Kirkwood expression or equivalent.

For equilibrium-state liquid surfaces, the surface tension γ can be calculated from $P_n(x)$ and $P_t(x)$ by

$$\gamma = \frac{1}{2}\int_0^L dx\left[P_n(x) - P_t(x)\right], \quad (19)$$

where $\frac{1}{2}$ in front of the integral is introduced due to the presence of the two interfaces at $x/L=0.25$ and $x/L=0.75$ [41]. The formula in Eq. (19) was applied to these nonequilibrium stationary states. Error bars were calculated as the standard deviation of the two surface tension values for the surface at $x/L=0.25$ (the integral from 0 to $L/2$) and that at $x/L=0.75$ (the integral from $L/2$ to L). The "surface tension" or γ values are presented in Table II. It is negative in the case of $a=0$. Surface tension is positive if the liquid system is at equilibrium, but this is not necessarily the case for a nonequilibrium state. Although the physical meaning of the computed γ quantities in these systems is not clear, they still provide a useful characterization of this boundary. As the value of a increases, $P_t(x)$ becomes flat as shown in Fig. 3(c′) and the surface tension decreases. The surface tension γ is essentially zero in the case of $a=0$.

The potential energy per particle U, defined as,

$$U = \left\langle \frac{1}{2N_k}\sum_{i\in k}\sum_{j\neq i}\phi(r_{ij})\right\rangle, \quad (20)$$

is shown in Fig. 5. In the case of $a=0$, shown in Fig. 5(a), there is a difference between the MD and HS treatments in U, just as for ρ, although oscillations are not present in the MD data this time. The HS-derived potential-energy profile is a step function just as is the kinetic temperature profile. In contrast, the potential-energy profile by the MD simulation changes smoothly even near the boundary. It takes about four molecular diameters to approach the bulk value of U from the boundary on either side. This is because the potential energy $U(x)$ at the position x is nonlocal in origin and depends on the $\rho(x')$ for $x' \neq x$ within a few molecular diameters of this position by virtue of the finite range of the pair potential. The profile $\rho(x)$ changes spatially noticeably in the transition zone between the two temperature extremes, and this is reflected in $U(x)$. The potential-energy $U(x)$ on the

TABLE II. Surface tension γ calculated by Eq. (19) in the cases of $a=0$, $a=1$, and $a=5$. The numbers in parentheses are the estimated uncertainties.

$a=0$	$a=1$	$a=5$
−0.013(4)	−0.008(10)	0.001(6)

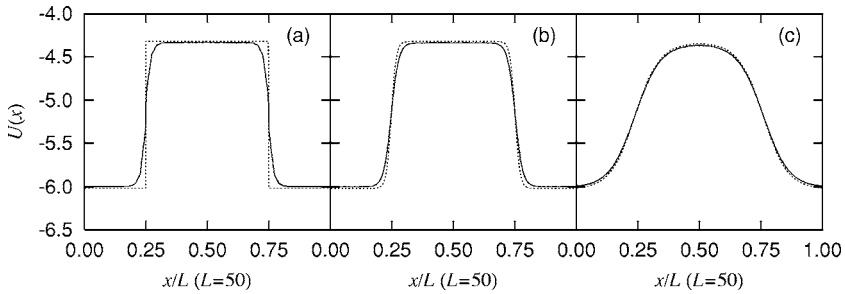

FIG. 5. Distributions of potential energy U as a function of x. See the caption of Fig. 2 for the details. In the case of $a=0$, the HS-derived profile is a stepwise function, whereas the MD-derived profile changes smoothly near the boundary. As the value of a increases the agreement between the two techniques improves significantly.

low density side is affected by the high density region near the boundary and vice versa. This is why the potential-energy profile by the MD simulation changes smoothly across the boundary even for $a=0$. As the value of a increases the MD and HS approaches give more similar profiles. In the case of $a=1$, there is still a difference of $U(x)$ as shown in Fig. 5(b). The two $U(x)$ profiles agree well when $a=5$, as revealed in Fig. 5(c).

The configurational temperature, T_{cfg}, was also calculated in this study. This definition of the temperature has its origins in a new approach by Rugh [42,43] which gives a definition for the temperature that has both kinetic and interaction parts. The special case using only the momenta is the usual formula for the kinetic temperature, T_{knt}. The other case that has only the interaction part is the configurational temperature T_{cfg} [44–47]. The configurational temperature T_{cfg} is defined by

$$\frac{1}{T_{\mathrm{cfg}}} = k_{\mathrm{B}} \left\langle \frac{\sum_{i\in k} \nabla_i^2 \sum_{j\neq i} \phi(r_{ij})}{\sum_{i\in k} \left[\nabla_i \sum_{j\neq i} \phi(r_{ij})\right]^2} \right\rangle. \tag{21}$$

At equilibrium the kinetic and configurational temperatures should give the same value, although the situation is less clear for nonequilibrium states, even if stationary. In the present systems we have an interfacial region as well, and so it is of interest to compute this quantity as a function of x.

The profile of configurational temperature T_{cfg} is shown in Fig. 6. In the case of $a=5$, T_{cfg} changes gradually and agrees with T_{knt} as shown in Fig. 6(c). The differences between T_{cfg} and T_{knt} are 1% or less. This slight difference probably comes from the limited number of particles in the sliced region. There are 170–230 particles in each sliced region. There is an inherent difference between T_{cfg} and T_{knt} of the order of $O(1/N)$. According to the bulk-system simulation [45], the difference between T_{cfg} and T_{knt} is also of the order of 1%. Therefore T_{cfg} agrees reasonably with T_{knt}, as can be seen in Fig. 6(c).

As the value of a decreases, differences between T_{cfg} and T_{knt} emerge. In the case of $a=0$, the configurational temperature T_{cfg} is different from its bulk value within two molecular diameters on either side of the boundary. This difference disappears and the two temperatures T_{cfg} and T_{knt} agree well with each other beyond a two-diameter zone near the boundary. The reason for this difference is presumably the same as for $U(x)$, in that the configurational temperature is a nonlocal property, and is not calculated solely by the particle configuration at x but depends also on the configuration of particles within the range of the pair potential up to a few molecular diameters away. Therefore T_{cfg} does not exhibit a sharp transition near the boundary, even for $a=0$. Although this feature is similar to U, T_{cfg} approaches its bulk value within a shorter distance from the boundary than U. The potential energy U takes four diameters to approach its bulk value, whereas T_{cfg} takes only about two diameters. This is probably because the power of inverse r_{ij} relevant for the dominant term of T_{cfg} is higher than for U. In the case of the LJ 12-6 fluid, U is given by the sum of the pair potential in Eq. (1). At long range, the attractive part of the potential, $1/r_{ij}^6$ dominates the sum for U, so,

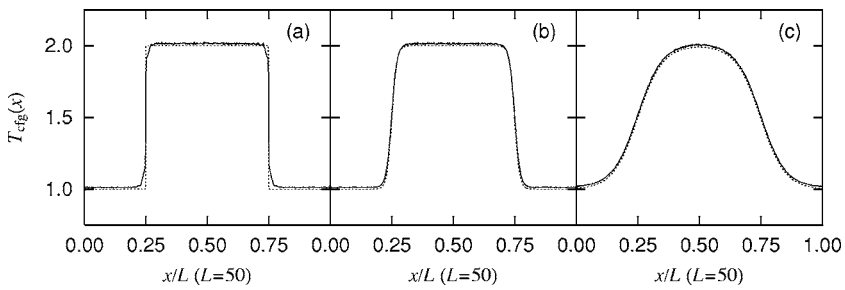

FIG. 6. Distributions of configurational temperature T_{cfg} calculated by the MD simulations. The dotted lines are kinetic temperature T_{knt} used as input in Eq. (6). In the case of $a=0$, T_{cfg} is different from its bulk value near the boundary. The differences between T_{cfg} and T_{knt} decreases with increasing value of a.

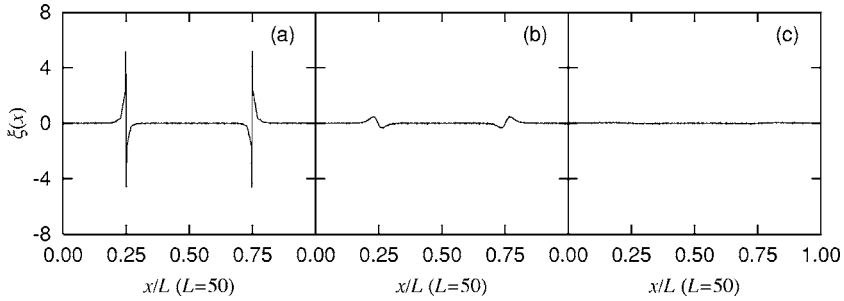

FIG. 7. Distributions of variable ξ for the Nosé-Hoover thermostat. Other details are given in the caption of Fig. 2. In the case of $a=0$, the profile has a negative peak on the high temperature side and a positive peak on the low temperature side near the boundary. As the value of a increases, all peaks become broader and lower.

$$U \sim \frac{1}{r_{ij}^6}. \tag{22}$$

As for T_{cfg}, the numerator in $\langle \cdots \rangle$ in Eq. (21) involves the second derivative of the potential,

$$\nabla_i^2 \sum_{j \neq i} \phi(r_{ij}) \sim \frac{1}{r_{ij}^8}. \tag{23}$$

The denominator in Eq. (21) consists of the square of the first derivative of the potential:

$$\left[\nabla_i \sum_{j \neq i} \phi(r_{ij}) \right]^2 \sim \frac{1}{r_{ij}^{14}}. \tag{24}$$

Therefore the numerator converges slower than the denominator and dominates the long distance behavior of T_{cfg}, which scales as $\sim r_{ij}^{-8}$. It is not only for the LJ 12-6 system that T_{cfg} converges faster than U, but for any algebraic potential the difference is the second power of r_{ij} [47]. This is why T_{cfg} approaches its bulk value at smaller distances from the boundary than U.

The fluid velocity, v_x, along the x-direction is given by

$$v_x = \left\langle \frac{1}{N_k} \sum_{i \in k} \dot{x}_i \right\rangle. \tag{25}$$

In all cases of $a=0$, 1, and 5, $v_x(x)$ derived by the MD simulation is statistically zero (as it is for the HS solution), indicating that the MD data were gathered after the system had reached a stationary state.

The x-profile for the variable ξ of the Nosé-Hoover thermostat used to control the temperature in Eqs. (3)–(5) is shown in Fig. 7. The variable ξ plotted in Fig. 7 is its time average in each sliced segment. It has a negative peak on the high temperature side and a positive peak on the low temperature side near the boundary in the case of $a=0$, as shown in Fig. 7(a). This is because the particles that came into the low temperature region from the high temperature region had to be cooled down, and those that came into the high temperature region from the low temperature region had to be heated up to achieve the ambient temperature. As the value of a increases, all peaks become broader and lower, as shown in Figs. 7(b) and 7(c) the two peaks have almost disappeared.

The average force acting on the particles in each "slice" of the histogram is shown in Fig. 8. Its x component, for example, is given by

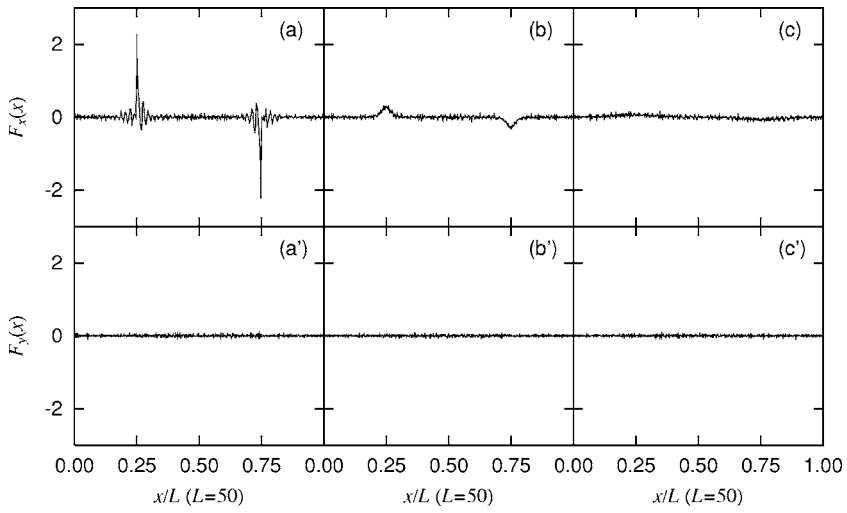

FIG. 8. (a)–(c) Distributions of x components of force F_x and (a′)–(c′) those of y components F_y. See the caption of Fig. 2 for the details. In the case of $a=0$, F_x has a positive peak at $x/L=0.25$ and a negative peak at $x/L=0.75$. As the value of a increases, all peaks become broader and lower. The y component of the force, F_y, is zero in all cases.

$$F_x = \left\langle -\sum_{i\in k}\sum_{j\neq i}\frac{\partial\phi(r_{ij})}{\partial x_i}\right\rangle, \tag{26}$$

which is shown in Figs. 8(a)–8(c). In the case of $a=0$, there is a positive peak at the boundary of $x/L=0.25$ and a negative peak at $x/L=0.75$. The density in the low-temperature region is higher than that in the high-temperature region. This local imbalance of particle density causes a net force to the right at the $x/L=0.25$ boundary and a net force to the left at the $x/L=0.75$ boundary. This is why there is a positive peak at the boundary of $x/L=0.25$ and a negative peak at $x/L=0.75$.

The y component F_y was also calculated by

$$F_y = \left\langle -\sum_{i\in k}\sum_{j\neq i}\frac{\partial\phi(r_{ij})}{\partial y_i}\right\rangle, \tag{27}$$

and shown in Figs. 8(a′)–8(c′). In all cases of $a=0$, 1, and 5, the F_y are statistically zero for all x as one would expect by symmetry. There is no net force along y for symmetry reasons as there is no temperature gradient in this direction. The z component F_z is zero for the same reason.

IV. CONCLUSIONS

We have investigated the validity of a hydrostatics description of a Lennard-Jones 12-6 liquid system in which a field gradient is constrained to vary on a truly molecular length scale. The system modeled is a nanochannel in which there is an enforced temperature gradient perpendicular to the channel axis. The "exact" solution is achieved using molecular dynamics (MD) and this is compared with the continuum hydrostatic and equation of state result (HS) for a stationary nonequilibrium state. The temperature profile has a region of high and low temperature separated by a transition region of varying degrees of sharpness, ranging from zero ($a=0$) to about ten ($a=5$) molecular diameters across. A systematic comparison was made between the spatial variation of the density ρ, pressure P, and potential energy U by the MD and HS methods. The normal component of the pressure tensor $P_n(x)$ is constant with x in all cases of a. It means that the MD-derived normal pressure fulfills the HS condition with no flow even at the molecular scale. On the other hand, the transverse component of the pressure $P_t(x)$ has peaks near the boundary. These pressure profiles are similar to those at the liquid-gas interface [38,40]. For a ten particle diameter transition region in temperature, the profiles for ρ and U properties calculated with the two techniques agreed well with each other. Differences between the two approaches were found for a transition length less than about two particle diameters. For a perfectly sharp transition in temperature, major differences between the MD and HS results were evident. Oscillations were observed near the boundary between the two temperature regions in the MD-derived density profile. The potential energy U profile was different (but not oscillatory). Also the configurational temperature T_{cfg} profile showed differences from the kinetic definition of the temperature. The MD-derived profile of U does not change as steeply as that by the HS calculation. The profile of T_{cfg} obtained by the MD simulation also does not change as steeply as that of the kinetic temperature, T_{knt}.

The field differences between the two techniques indicate the invalidity of the HS where the temperature changes significantly over one or two molecular diameters, and by of order one reduced unit. In other words, the hydrodynamic Navier-Stokes description is reliable down to the nanometer scale for a characteristic temperature gradient of $dT/dx=0.1$ (or $a=5$). This temperature gradient corresponds to $dT/dx=3.5$ K/Å in the case of argon, using its LJ parameters [48]. While such large temperature gradients are not typical for experimental systems, they could conceivably be achieved using laser technology. Temperature control is a significant issue in nanoscale devices and the present study has provided some insights into the range of applicability of two modeling approaches that could be used. Based on these results, it can be concluded that MD could be replaced by the continuum approach to study nonequilibrium liquid behavior, reducing considerably the computational cost, if the transition range between the temperature extremes is greater than about ten molecular diameters for a simple liquid. The HS treatment can be used on longer length scales, and this approach could therefore still be useful in the area of microfluidics. As for complex liquids such as ionic liquids and polymers, such a transition range could be different for different model fluids and would be an interesting theme for a future work.

ACKNOWLEDGMENT

This work was supported by the Grant-in-Aid for Scientific Research (Grant No. 17740260) from the Ministry of Education, Culture, Sports, Science and Technology, Japan.

[1] D. C. Rapaport, Phys. Rev. Lett. **60**, 2480 (1988).
[2] D. C. Rapaport, Phys. Rev. A **43**, 7046 (1991).
[3] M. Mareschal, M. Malek Mansour, A. Puhl, and E. Kestemont, Phys. Rev. Lett. **61**, 2550 (1988).
[4] A. Puhl, M. M. Mansour, and M. Mareschal, Phys. Rev. A **40**, 1999 (1989).
[5] D. Hirshfeld and D. C. Rapaport, Phys. Rev. Lett. **80**, 5337 (1998).
[6] D. Hirshfeld and D. C. Rapaport, Phys. Rev. E **61**, R21 (2000).
[7] B. L. Holian, W. G. Hoover, B. Moran, and G. K. Straub, Phys. Rev. A **22**, 2798 (1980).
[8] B. L. Holian, C. W. Patterson, M. Mareschal, and E. Salomons, Phys. Rev. E **47**, R24 (1993).
[9] J. Bougie, Sung Joon Moon, J. B. Swift, and H. L. Swinney, Phys. Rev. E **66**, 051301 (2002).
[10] H. Okumura and D. M. Heyes, Phys. Rev. E **70**, 061206 (2004).

[11] C. Xiao, D. M. Heyes, and J. G. Powles, Mol. Phys. **100**, 595 (2002).
[12] H. Okumura and N. Ito, Phys. Rev. E **67**, 045301(R) (2003).
[13] K. P. Travis, B. D. Todd, and D. J. Evans, Phys. Rev. E **55**, 4288 (1997).
[14] K. P. Travis and K. E. Gubbins, J. Chem. Phys. **112**, 1984 (2000).
[15] B. D. Todd, D. J. Evans, and P. J. Daivis, Phys. Rev. E **52**, 1627 (1995).
[16] D. C. Rapaport, Phys. Rev. A **36**, 3288 (1987).
[17] S. T. Cui and D. J. Evans, Mol. Simul. **9**, 179 (1992).
[18] D. Risso and P. Cordero, Phys. Rev. E **58**, 546 (1998).
[19] D. R. J. Monaghan and G. P. Morriss, Phys. Rev. E **56**, 476 (1997).
[20] J. Delhommelle, J. Petravic, and D. J. Evans, J. Chem. Phys. **119**, 11005 (2003).
[21] K. Kadau, T. C. Germann, N. G. Hadjiconstantinou, P. S. Lomdahl, G. Dimonte, B. L. Holian, and B. J. Alder, Proc. Natl. Acad. Sci. U.S.A. **101**, 5851 (2004).
[22] S. P. Karlov, D. A. Kazenin, B. I. Myznikova, and I. I. Wertgeim, J. Non-Equilib. Thermodyn. **30**, 283 (2005).
[23] J. Neumann and R. Brinkmann, J. Biomed. Opt. **10**, 024001 (2005).
[24] H. Okumura and F. Yonezawa, J. Chem. Phys. **113**, 9162 (2000).
[25] H. Okumura and F. Yonezawa, J. Phys. Soc. Jpn. **70**, 1990 (2001).
[26] S. Nosé, Mol. Phys. **52**, 255 (1984).
[27] S. Nosé, J. Chem. Phys. **81**, 511 (1984).
[28] W. G. Hoover, Phys. Rev. A **31**, 1695 (1985).
[29] G. J. Martyna, M. E. Tuckerman, D. J. Tobias, and M. L. Klein, Mol. Phys. **87**, 1117 (1996).
[30] J. K. Johnson, J. A. Zollweg, and K. E. Gubbins, Mol. Phys. **78**, 591 (1993).
[31] T. Sun and A. S. Teja, J. Phys. Chem. **100**, 17365 (1996).
[32] H. Okumura and Y. Okamoto, J. Comput. Chem. **27**, 379 (2006).
[33] T. Murakami, T. Shimada, S. Yukawa, and N. Ito, J. Phys. Soc. Jpn. **72**, 1049 (2003).
[34] L. Xue, P. Keblinski, S. R. Phillpot, S. U.-S. Choi, and J. A. Eastman, Int. J. Heat Mass Transfer **47**, 4277 (2004).
[35] J. Delhommelle and D. J. Evans, J. Chem. Phys. **114**, 6229 (2001).
[36] P. Geysermans, N. Elyeznasni, and V. Russier, J. Chem. Phys. **123**, 204711 (2005).
[37] J. H. Irving and J. G. Kirkwood, J. Chem. Phys. **18**, 817 (1950).
[38] J. P. R. B. Walton, D. J. Tildesley, J. S. Rowlinson, and J. R. Henderson, Mol. Phys. **48**, 1357 (1983).
[39] B. Hafskjold and T. Ikeshoji, Phys. Rev. E **66**, 011203 (2002).
[40] T. Ikeshoji, B. Hafskjold, and H. Furuholt, Mol. Simul. **29**, 101 (2003).
[41] J. G. Kirkwood and F. P. Buff, J. Chem. Phys. **17**, 338 (1949).
[42] H. H. Rugh, Phys. Rev. Lett. **78**, 772 (1997).
[43] H. H. Rugh, J. Phys. A **731**, 7761 (1998).
[44] B. D. Butler, G. Ayton, O. G. Jepps, and D. J. Evans, J. Chem. Phys. **109**, 6519 (1998).
[45] O. G. Jepps, G. Ayton, and D. J. Evans, Phys. Rev. E **62**, 4757 (2000).
[46] G. Rickayzen and J. G. Powles, J. Chem. Phys. **114**, 4333 (2001).
[47] J. G. Powles, G. Rickayzen, and D. M. Heyes, Mol. Phys. **103**, 1361 (2005).
[48] J.-P. Hansen and I. R. McDonald, *Theory of Simple Liquids*, 2nd ed. (Academic, London, 1986), p. 72.